J. Fluid Mech. (1988), *vol.* 196, *pp.* 263–290
Printed in Great Britain

Time-periodic convection in porous media: transition mechanism

By PAUL H. STEEN† AND CYRUS K. AIDUN‡

†School of Chemical Engineering and Mathematical Sciences Institute, Cornell University, Ithaca, NY 14853, USA

‡Engineering Division, Institute of Paper Chemistry, P.O. Box 1039, Appleton, WI 54912, USA

(Received 22 September 1987 and in revised form 14 April 1988)

We resolve the disturbance structures that destabilize steady convection rolls in favour of a time-periodic pattern in two-dimensional containers of fluid-saturated porous material. Analysis of these structures shows that instability occurs as a travelling wave propagating in a closed loop outside the nearly motionless core. The travelling wave consists of five pairs of thermal cells and four pairs of vorticity disturbances in the case of a square container. The wave speed of the thermal disturbances is determined by an average base-state velocity and their structure by a balance between convection and thermal diffusion. Interpretation of the 'exact' solution is aided by a one-dimensional convection-loop model which correlates (i) point of transition, (ii) disturbance wavenumber, and (iii) oscillation frequency given the base-state temperature and velocity profiles. The resulting modified Mathieu–Hill equation clarifies the role of the vertical pressure gradient, induced by the impenetrable walls, and the role of the base-state thermal layer.

1. Introduction

When heated moderately from below, a closed container filled with a fluid-saturated porous material exhibits a transition from steady to time-periodic convection as the temperature difference across the container (a Rayleigh number R) is increased. We study this steady-to-oscillatory transition for two-dimensional motions in rectangular containers with emphasis on the square container.

Using an eigenfunction expansion in conjunction with a numerical branch-tracing technique for the square box we have previously obtained (i) the point of transition to time-periodicity, $R_p = 390.7$, (ii) the frequency of oscillation at transition, $\Omega_p = 82.8$ cycles per dimensionless time, and (iii) the detailed structure of the destabilizing disturbance, results that have been reported in summary form (Aidun & Steen 1986, 1987). The value $380 \leqslant R_p \leqslant 400$ has been known for some time (Caltagirone 1974; Schubert & Straus 1982) and the frequency of oscillation at transition has recently been confirmed independently (Kimura, Schubert & Straus 1987). The results (iii) are new as far as we are aware, made possible by our numerical approach which is distinguished from more conventional finite-difference, finite-element, spectral, and pseudo-spectral methods by its ability to capture the structure of infinitesimal destabilizing disturbances at points of bifurcation.

The structure delivered by the 'exact' solution shows a number of disturbance cells that propagate with the base flow in a closed loop around the square domain. The size and strength of the cells varies with position around the loop. To aid in capturing the heart of the physics and to hone our understanding of the instability, we seek a model that can predict (i) the point of instability, (ii) the frequency of the disturbance and (iii) the wavenumber of the disturbance given a simple measure of the growth and distortion of the base flow as it depends on Rayleigh parameter. The model we develop is a convection–diffusion equation on a one-dimensional domain, the circle. The model's success in predicting properties (i), (ii) and (iii) as they depend on the aspect ratio of the container is qualified only by the somewhat *ad hoc* nature of steps involved in its derivation.

Previous investigations, both experimental and numerical, have considered the oscillatory instability within two contexts: the saturated porous medium and the Hele-Shaw cell. The formal correspondence between the porous medium and the Hele-Shaw problems has severe limitations which have been discussed in the literature (Hartline & Lister 1977; Kvernvold 1979; Frick & Clever 1982; Koster & Muller 1982); however, for the oscillatory transitions that we consider the two systems are in a range of parameters for which the correspondence is close, if not exact.

Early experiments concerning the transition from steady to time-periodic motion came from those studying convection in the porous-media system. Combarnous & Lefur (1969) seem to have first observed a 'fluctuating' state in experiment and thereby inferred such a transition. Further observations in saturated porous beds (Caltagirone, Cloupeau & Combarnous 1971) and in the Hele-Shaw cell (Horne & O'Sullivan 1974) established that the convection patterns both below and above the transition can be two-dimensional; a two-dimensional fluctuating motion can replace a steady roll-cell. More recent experiments in Hele-Shaw slots (Koster & Muller 1980, 1981, 1982, 1984) provide more details of this and higher transitions. Noteworthy among Koster & Muller's observations is the identification within the regime of time-periodic flow of at least two types of oscillations distinguished by different structures. This supports results from the numerical work of Caltagirone (1975), Horne & Caltagirone (1980) and Frick & Muller (1983) who report that qualitatively different oscillatory motions can be realized for fixed values of the parameters; the motion that is selected depends on 'initial conditions'. Frick & Muller (1983) indicate that one type of calculated oscillation grows from a small-amplitude sinusoidal variation at the onset of time-dependence while the other type is consistently characterized by large-amplitude oscillations. These two numerically predicted motions are matched to two oscillating structures which have been observed in particular experiments. The Frick & Muller (1983) work is noteworthy for the tight correspondence drawn between experiment and simulation.

The oscillations we analyse are limited to those that arise from instabilities of the 'primary' branch of steady convection patterns. A thought experiment defines the notion of primary branch. Suppose we slowly increase the Rayleigh parameter from below convection onset and suppose that we can shield our system from all but infinitesimal disturbances. There will be a first transition R_c to a steady roll-cell pattern (Lapwood 1948) which will subsequently grow in strength and distort as the Rayleigh number is raised. We call this set of patterns the primary branch of solutions. The system will remain stable until a second transition R_p where an oscillatory motion will replace the steady finite-amplitude roll-cell. The second transition from the primary branch is always one to a time-periodic motion. It is well known for a two-dimensional system that the horizontally *unconfined* layer is susceptible to only 'Eckhaus' (or 'sideband') and oscillatory instabilities (Kvernvold 1979). However, for a system with sidewalls the Eckhaus instability manifests itself as an instability to finite-amplitude disturbances; the sidewalls allow only discrete wavenumbers and the sideband instability is thereby filtered. Therefore, although all the convection patterns we study are stable to small disturbances below transition, in many cases they are not stable to finite-amplitude disturbances there; these physically relevant finite-amplitude instabilities are not treated here. Furthermore, this study does not consider instabilities of steady patterns on branches that are not connected to the conduction solution. Of course, stable time-periodic motions can arise through means other than transitions from steady patterns; these motions are also not considered.

Relevant numerical studies are more numerous than the extant experimental observations which have been highlighted above. Caltagirone (1974, 1975), motivated by the observations of Combarnous & LeFur (1969) and Caltagirone, Cloupeau & Combarnous (1971), mapped out the boundary of instability to oscillations as a function of aspect ratio of the rectangular container using a Galerkin technique. In addition, by solving many initial-value problems using a finite-difference scheme, he obtained the structure of fluctuating patterns above the stability boundary. Although Caltagirone (1975) identifies the thermal boundary layer as source of the destabilizing disturbance, he neither resolves the detailed structure, nor reports wavenumbers or frequencies. Horne & O'Sullivan (1974) solve for the fluctuating states using a finite-difference technique. They describe the instability process as an interaction between the unstable thermal layer at the bottom of the box and the descending thermal disturbances consisting of cold parcels of fluid coming from the unstable layer at the top of the box. The arrival of the cold fluid is said to 'trigger' the disturbance in the warmer layer. In an ingenious attempt to distinguish the importance of triggering relative to thermal-layer instabilities, Horne & O'Sullivan (1978) calculate the motions in a rectangle with a permeable top and compare the periods and regularity of fluctuations with the case of the impermeable top. They conclude that an unstable thermal layer is essential to the instability and that the interaction with descending disturbances contributes to the regularity of the motion. For a Rayleigh number somewhat above the stability boundary, Horne & Caltagirone (1980) find that the point of origin of the instability in the thermal boundary layer determines which of two possible fluctuating states will be realized. One state consists of regular (periodic) and the other 'irregular' oscillations.

All these studies attempt to uncover from various perspectives the physical mechanism that is responsible for transition and these efforts develop a reasonably detailed understanding of the transition dynamics. Indeed, given that the principal tool employed in all these investigations is the solution of initial-boundary-value problems, via various finite-difference schemes, repeated over and over for various initial conditions, the resulting picture gives as much detail as can be expected. Yet characteristics at the heart of the transition process such as thermal-disturbance size and its relationship to frequency and to the particular point of instability in Rayleigh number are barely addressed. Our resolution of the disturbance structure, obtained by calculating the eigenfunctions corresponding to the critical eigenvalue of the linear operator governing small disturbances from the base state, opens the way for an analysis which first relates oscillation frequency to base-state velocities through disturbance size (wavelength), and then determines thermal-disturbance size as a balance between convection of the base-state temperature profile by disturbance velocities and diffusion of the thermal disturbances by conduction.

The numerical work of Schubert & Straus (1982) and Kimura, Schubert & Straus (1986, 1987) has been primarily concerned with uncovering routes to chaos in the context of two-dimensional porous-media convection. Although little attention has been paid to the underlying physical transition mechanism, they have accurately located the transition point and frequency of oscillation at transition to time-dependence as well as corresponding characteristics at a sequence of higher transitions.

After formulating the problem we outline the numerical method employed and review the 'exact' solution thereby obtained. On the basis of the numbers delivered by the 'exact' solution we justify splitting the linear disturbance equation into two separate balances: one a first-order wave equation that governs propagation of disturbances and the other a second-order elliptic equation that determines the structure of disturbances. This empirical observation is the key to the simplification provided by the model. The two equations decouple. Given a time-independent solution to the structure equation, the propagation equation can be solved using that structure as an initial condition.

Attention turns next to the structure equation and model construction proceeds in two stages. The disturbance velocity has contributions from the disturbance buoyancy force and the disturbance pressure force and Model I, the first stage, neglects the influence of the pressure force. The structure equation is transformed from the two-dimensional square domain to a one-dimensional loop domain. The result is a Mathieu–Hill equation on the circle for the temperature disturbance. Here the Rayleigh number plays the role of natural wavenumber and parametric excitation is due to the vertical component of the base-state temperature gradient. The requirement that the disturbances must fit on the circle (i.e. be periodic) can only be met for certain Rayleigh numbers and base-state temperature gradients, values at which diffusion of disturbances is just balanced by convection of the base-state profile. Model I correctly predicts the wavenumber of the disturbance and gives a reasonable estimate of the base-state temperature gradient *given* the critical Rayleigh number. However, it cannot predict the critical Rayleigh number.

Model II, the second stage of model construction, takes account of the pressure contribution to disturbance velocity. This effect shifts the spatial phase relationship between diffusion and convection and eliminates periodic solutions which otherwise exist at lower Rayleigh numbers. A modified Mathieu–Hill equation emerges. It predicts wavenumber *and* critical Rayleigh number given the development of the base-state temperature profile. The frequency of the disturbance is then obtained from the propagation equation given the dependence of base-state velocity on Rayleigh parameter.

2. Formulation

Two planes separated by a gap l are arranged horizontally relative to gravity g; the gap is filled with a porous material and saturated with a fluid of viscosity ν. The bottom plate is held isothermally at a temperature ΔT greater than the cooler isothermal top plate. For motions with low Reynolds numbers based on pore size, arbitrary deviations in velocity $\boldsymbol{v}$, temperature θ, and pressure p from the motionless conduction state are governed by

$$\nabla \cdot \boldsymbol{v} = 0, \tag{1a}$$

$$\boldsymbol{0} = -\nabla p - \boldsymbol{v} + R^{\frac{1}{2}}\theta \boldsymbol{k}, \tag{1b}$$

$$\frac{\partial \theta}{\partial t} + R^{\frac{1}{2}}\boldsymbol{v} \cdot (\nabla \theta - \boldsymbol{k}) = \nabla^2 \theta. \tag{1c}$$

The inertia term in the momentum equation (1*b*) has been neglected since it is proportional to the permeability K of the porous material which enters through Darcy's law and which is typically very small. The Boussinesq approximation couples the momentum equation (1*b*) to the energy equation (1*c*) and the Rayleigh number $R \equiv g\beta \Delta T K l/\kappa_{\mathrm{m}} \nu$ gives a measure of the coupling. Here β is the coefficient of thermal expansion of the fluid and κ_{m} is the effective fluid/solid thermal diffusivity. $\boldsymbol{k}$ is a unit vector directed oppositly to gravity.

Scales of length l, velocity $R^{\frac{1}{2}}\kappa_{\mathrm{m}}/l$, temperature ΔT, and time $l^2 H/\kappa_{\mathrm{m}}$ are employed; $H \equiv \rho_{\mathrm{m}} C_{p\mathrm{m}}/\rho_{\mathrm{f}} C_{p\mathrm{f}}$ is the ratio of the heat capacity of the fluid–solid mixture to that of the fluid.

The layer is confined by two vertical insulating walls separated by a distance hl which define a rectangular container of aspect ratio h. The boundary conditions, in summary, are specified by an isothermal top and bottom, insulated sidewalls, and no penetration of all containing walls.

System (1) can readily be re-expressed as a scalar integro-differential equation for the disturbance temperature

$$\frac{\partial \theta}{\partial t} + R(\theta \boldsymbol{k} + \nabla[\mathrm{G}^*(\nabla\theta \cdot \boldsymbol{k})]) \cdot (\nabla\theta - \boldsymbol{k}) = \nabla^2\theta, \tag{2}$$

where the Poisson equation with Neumann boundary conditions,

$$-\nabla^2 p = f, \tag{3a}$$

$$\frac{\partial p}{\partial n} = 0 \quad \text{on all boundaries,} \tag{3b}$$

has solution

$$p = -\mathrm{G}^* f, \tag{4}$$

which defines the integral operator G. For equation (2) the inhomogeneous term in (3*a*) takes the form $f = R^{\frac{1}{2}} \partial\theta/\partial y$. An explicit form of the integral operator is easily found after noting that p is the superposition of terms that are products of a cosine dependence in x and a cosine dependence in y. Here we have used a Cartesian coordinate system with horizontal coordinate x, vertical coordinate y and origin such that the sidewalls are at $x = \pm\frac{1}{2}h$ and the bottom and top are at $y = 0$, 1. The linearized version of (2) has eigenfunctions (Beck 1972)

$$\theta_i \equiv \cos[(m\pi/h)(x + \tfrac{1}{2}h)] \sin n\pi y, \tag{5i}$$

and corresponding eigenvalues

$$R_i \equiv \pi^2\left[\left(\frac{m}{h}\right)^2 + n^2\right] \Big/ \left[1 - n^2 \Big/ \left(\left(\frac{m}{h}\right)^2 + n^2\right)\right], \tag{6i}$$

where $\quad m = 0, 1, 2, \ldots, n = 1, 2 \ldots \quad$ and $\quad i = [m, n]$.

The numbering of equations (5*i*) and (6*i*) where $i = 1, \ldots, \infty$ is an enumeration of the wavenumber pairs $[m, n]$ which distinguishes each member of the infinite set of equations represented.

A further transformation of the system uses the solutions to the linearized problem (5*i*) in an eigenfunction expansion,

$$\theta(x, y, t) = \sum_{i=1}^{\infty} a_i(t)\, \theta_i(x, y). \tag{7}$$

Substituting (7) into (2), taking projections on each of the modes ($5i$), and using the self-adjoint property of the linearized equation to eliminate the $\nabla^2\theta$-term following Rosenblat (1979), yields an infinite system of ordinary differential equations formally equivalent to system (1),

$$\frac{\mathrm{d}a_i}{\mathrm{d}t} = \lambda_i(R-R_i)\,a_i + RA_{ijk}\,a_j\,a_k, \qquad (8i)$$

$$i = 1, 2, \ldots, \infty.$$

The constants λ_i and A_{ijk} are known in closed form as functions of h and can be found in Steen (1986). The first term gives the growth (decay) of the ith mode due to its linear instability (stability) and the quadratic term accounts for nonlinear mixing; the implied sum over modes j and k extends over all pairs (j, k).

For future use we record the special case of system (1) which governs infinitesimal disturbances $\hat{\boldsymbol{v}}$, $\hat{\theta}$, $\hat{p}$ from a known steady solution $\bar{\boldsymbol{v}}$, $\bar{\theta}$, $\bar{p}$ of equations (1). Substitute

$$\boldsymbol{v} \equiv \bar{\boldsymbol{v}} + \epsilon\hat{\boldsymbol{v}}, \quad \theta \equiv \bar{\theta} + \epsilon\hat{\theta}, \quad p \equiv \bar{p} + \epsilon\hat{p}, \qquad (9a, b, c)$$

into (1) and neglect $O(\epsilon^2)$-terms to obtain

$$\boldsymbol{\nabla}\cdot\hat{\boldsymbol{v}} = 0, \qquad (10a)$$

$$0 = -\boldsymbol{\nabla}\hat{p} - \hat{\boldsymbol{v}} + R^{\frac{1}{2}}\hat{\theta}\boldsymbol{k}, \qquad (10b)$$

$$\frac{\partial\hat{\theta}}{\partial t} + R^{\frac{1}{2}}\hat{\boldsymbol{v}}\cdot(\boldsymbol{\nabla}\bar{\theta} - \boldsymbol{k}) + R^{\frac{1}{2}}\bar{\boldsymbol{v}}\cdot\boldsymbol{\nabla}\hat{\theta} = \nabla^2\hat{\theta}. \qquad (10c)$$

3. Numerical method

The infinite system ($8i$, $i = 1, \infty$) is truncated to an M-dimensional system ($8i$, $i = 1, M$) by a strategy to be discussed below and the finite-dimensional system is treated as a bifurcation problem. Branches of steady solutions are curves in the ($M+1$)-dimensional space of components versus Rayleigh parameter. Given a point on a branch, i.e. a solution at a particular Rayleigh number, neighbouring points are approximated by a pseudoarclength continuation method (Keller 1977; Doedel 1980) and are calculated as solutions of the nonlinear algebraic system obtained by setting the time-derivatives in system ($8i$, $i = 1, M$) to zero. These computations are performed using the code AUTO, a package for continuation and bifurcation problems in ordinary differential equations developed by Doedel (1980). The arclength-like parameterization allows turning points to be handled routinely.

A calculation independent of the arclength continuation is used to test for stability at each point along the branch. The nonlinear system ($8i$, $i = 1, M$) is linearized about the known solution and the exponential growth or decay predicted by this linear operator is examined in the standard way. Instability is signalled when at least one growth parameter (eigenvalue) has a real part which changes from negative to positive along a previously stable branch. The eigenvector(s) associated with the critical eigenvalue(s) gives (give) the structure of the destabilizing disturbance(s); this is the structure associated with the new branch emanating from the bifurcation point. The stability calculation therefore involves calculating the eigenvalues and eigenfunctions of a linear system and is performed by a standard solver called from the AUTO package.

We start the branch-tracing procedure on the null solution at a Rayleigh value where it is stable. For the square box the first instability occurs at $R_c = 4\pi^2$ where

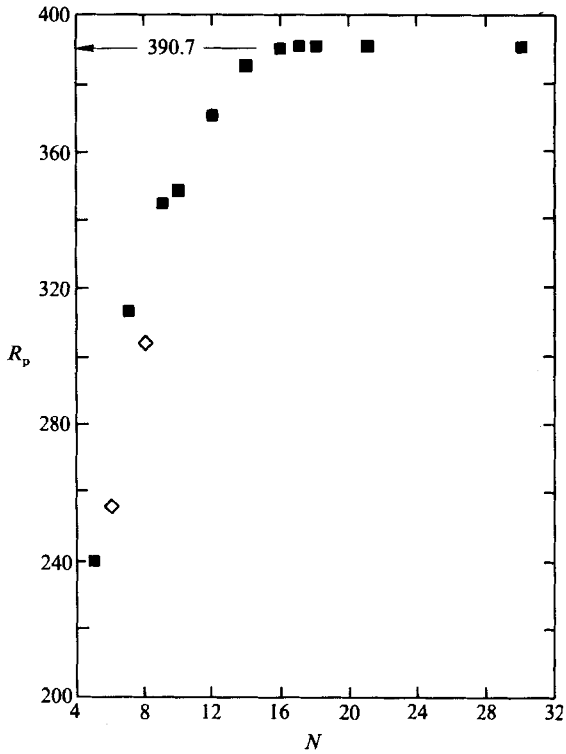

FIGURE 1. The Rayleigh number at instability of the primary branch R_p verses order of truncation N as obtained from the numerical computations for the square box. The squares are Hopf bifurcations and the diamonds are turning-point instabilities.

a single real eigenvalue becomes positive and the corresponding eigenvector indicates a structure with wavenumbers $[m, n] = [1, 1]$ (cf. equation (6*i*) with $h = 1$); results of linear theory are recovered at this step. The AUTO code is instructed to switch branches here to follow the growth of the steady single roll-cell which characterizes the primary branch. This branch remains stable until $R_p = 390.7$ where a complex-conjugate pair of eigenvalues cross the imaginary axis in the complex plane. The imaginary part yields the frequency of oscillation of the disturbance. The eigenvectors corresponding to this Hopf bifurcation span a two-dimensional subspace within the phase space of system $(8i,\ i = 1,\ M)$ and deliver the destabilizing disturbance structure of interest.

So far, assuming sufficiently accurate numerics, the only approximation to the original governing system (1) comes with the truncation to a finite number of modes. Our truncation scheme is guided by requirements (i) that sufficiently small wavelengths be included so as to capture the disturbance structure, and (ii) that the total energy of the system be conserved. As described in Aidun & Steen (1987) requirement (ii) leads to a rectangular cutoff form where all terms with $m \leqslant N$ and $n \leqslant N$ are kept (the order of the truncation N is related to the number of equations $M = \frac{1}{2}N(N+1)$). Requirement (i) is met by increasing N until the point of bifurcation and the disturbance structure are negligibly influenced by further increases in N. Figure 1 shows how overtruncation can affect the numerical prediction of instability. Not only does the maximum wavenumber strongly influence the Rayleigh value R_p at which the Hopf bifurcation is predicted for

		Present results		Caltagirone (1975)	
R	h	Nu	$\psi_{\max}$	Nu	$\psi_{\max}$†
50	0.50	1.00	0.000	1.0	0.0
	0.67	1.15	0.140	—	—
	0.75	1.39	0.270	—	—
	1.00	1.44	0.300	1.45	0.299
	1.50	1.15	0.213	—	—
100	0.50	2.14	0.281	2.136	0.28
	0.67	2.60	0.412	—	—
	0.75	2.65	0.457	—	—
	1.00	2.65	0.538	2.651	0.538
	1.50	2.31	0.566	2.314	0.568
150	0.50	3.24	0.379	—	—
	0.67	3.42	0.487	—	—
	0.75	3.42	0.526	—	—
	1.00	3.32	0.603	—	—
	1.50	2.93	0.646	—	—
200	0.50	4.03	0.424	4.026	0.424
	0.67	4.00	0.524	—	—
	0.75	3.96	0.560	—	—
	1.00	3.81	0.633	3.813	0.632
	1.50	3.38	0.683	3.381	0.683
250	0.50	4.58	0.452	—	—
	0.67	4.45	0.545	—	—
	0.75	4.39	0.579	—	—
	1.00	4.19	0.648	4.199	0.648
	1.50	3.73	0.702	3.731	0.702
300	0.50	5.02	0.471	5.016	0.471
	0.67	4.82	0.560	—	—
	0.75	4.73	0.592	—	—
	1.00	4.52	0.658	4.523	0.658
	1.50	4.02	0.713	4.032	0.715
350	0.50	5.38	0.485	—	—
	0.67	5.12	0.570	—	—
	0.75	5.04	0.601	—	—
	1.00	4.79	0.664	—	—
	1.50	(4.26)	(0.720)	—	—
400	0.50	5.69	0.495	—	—
	0.67	5.40	0.577	—	—
	0.75	5.31	0.607	—	—
	1.00	(5.03)	(0.668)	—	—
	1.50	(4.48)	(0.724)	—	—
450	0.50	5.96	0.503	—	—
	0.67	5.65	0.583	—	—
	0.75	5.54	0.613	—	—
	1.00	(5.25)	(0.671)	—	—
500	0.50	6.20	0.510	—	—
	0.67	5.88	0.588	—	—
	0.75	5.76	0.616	—	—
550	0.50	6.43	0.515	—	—
	0.67	6.09	0.592	—	—
	0.75	(5.97)	(0.619)	—	—

TABLE 1 (*continued on facing page*).

		Present results		Caltagirone (1975)	
R	h	Nu	$\psi_{\max}$	Nu	$\psi_{\max}$†
600	0.50	6.63	0.520	—	—
	0.67	(6.28)	(0.595)	—	—
	0.75	(6.15)	(0.622)	—	—
650	0.50	6.83	0.524	—	—
	0.67	(6.46)	(0.598)	—	—
700	0.50	7.01	0.528	—	—
	0.67	(6.63)	(0.600)	—	—
750	0.50	7.18	0.531	—	—
	0.67	(6.8)	(6.02)	—	—
800	0.50	7.34	0.534	7.345	0.533
	0.67	(6.94)	(0.603)	—	—
850	0.50	(7.49)	(0.536)	—	—
900	0.50	(7.64)	(0.538)	—	—
950	0.50	(7.78)	(0.540)	—	—
1000	0.50	(7.91)	(0.542)	—	—

† The maximum value of the stream function is rescaled by $R^{\frac{1}{2}}$.

TABLE 1. Comparison of the Nusselt number Nu and maximum value of the stream function of the base state from our calculations with those of Caltagirone (1975) for various aspects ratios h at a sequence of Rayleigh numbers R. Parentheses indicate an unstable base state.

$5 \leqslant N \leqslant 16$, but at $N = 6$ and $N = 8$ a qualitatively different transition via a turning point is predicted. This adds to the widespread evidence of the dangers of overtruncation.

A further check on the accuracy of the numerical method comes in comparing the Nusselt number and the maximum value of the stream function $\psi_{\max}$ for steady patterns on the primary branch with those reported by Caltagirone (1975) from his finite-difference calculation. Wherever comparison is possible, as listed in table 1, the agreement between results is within 0.5%. Caltagirone used a 32 × 32 mesh system for $R = 50$ and $R = 100$ and a 48 × 48 system for all other R.

To check the accuracy of the calculated disturbance quantities we reconstruct the terms appearing in the disturbance equations (10) from their Galerkin approximations ($N = 18$) and find that (10) are satisfied pointwise to within 5% everywhere in the box. The ten leading contributions to the two eigenvectors which characterize disturbances and their associated modeforms are listed in table 2. In summary, although the steps leading to the system (8*i*) are purely formal, solution of that system yields a temperature field $\theta(x, y; t)$ which satisfies the original governing equation (2) pointwise in the box at each time to within 5%. On this basis we have heretofore referred to it as the 'exact' solution where the quotation marks reflect the degree of inaccuracy. However, we now drop the quotation marks.

Our choice of basis functions for the Galerkin expansion, our selection of a truncation with a rectangular rather than a triangular form, and our use of the same set of functions both to calculate the base state and to capture the disturbance structure all add inefficiencies to the method. On the other hand, the basis chosen allows all nonlinear interactions and spatial derivatives to be evaluated exactly for

Eigenvector 1		Eigenvector 2	
Mode	Amplitude	Mode	Amplitude
[4,2]	0.623	[1,3]	0.887
[2,4]	−0.579	[3,3]	0.746
[4,4]	0.477	[3,5]	0.463
[0,4]	−0.445	[2,2]	0.402
[2,2]	0.432	[6,4]	−0.247

TABLE 2. The five largest components by amplitude and corresponding modes for the two eigenvectors that span the subspace where the Hopf bifurcation occurs

Aspect ratio h	R_p	Ω_p/R_p
0.5	825.7	1.7086
0.67	569.9	1.4759
0.75	506.1	1.4453
1.0	390.7	1.3308
1.5	309.5	1.0400

TABLE 3. Results of Rayleigh number R_p and frequency Ω_p at the onset of oscillation for various aspect ratios, from the exact solutions

all aspect ratios. Furthermore the rectangular form of cutoff allows overall conservation of energy, and a single truncation set allows base states to be as detailed as disturbance structures. All contribute to the accuracy of the method. Here, we trade computing time and storage space for accuracy. Neither of the former are limiting factors in these two-dimensional computations.

4. Exact solution

The development of the steady base flow as measured by the heat transfer (Nusselt number) and the maximum value of the stream function are indicated in table 1 for five aspect ratios, $0.5 \leqslant h \leqslant 1.5$. The point of instability R_p and oscillation frequency Ω_p are listed in table 3. Caltagirone's (1975) estimates for containers other than the square box are consistent with these values. The stabilization which occurs with decreasing aspect ratio is expected since the smaller the container in horizontal extent the larger the driving force needed to produce thermal gradients in the base flow sufficiently large for instability.

The structure of the base flow and temperature field at oscillation onset are shown in the centre plot of figures 2(*a*) and 2(*b*), respectively. The flow circulates clockwise and accelerates sharply at the upper right and lower left corners after rejecting and accepting heat along the top and bottom surfaces. The cold downflow compresses the thermal boundary layer at the bottom right corner and in conjunction with the hot upflow from the opposite corner establishes a stably stratified core region (Figure 2*b*, centre).

The destabilizing disturbance streamlines (figure 2*a*) and isotherms (figure 2*b*) are shown in clockwise progression around the figure at intervals of $\frac{1}{8}$ of one oscillation

(*a*)

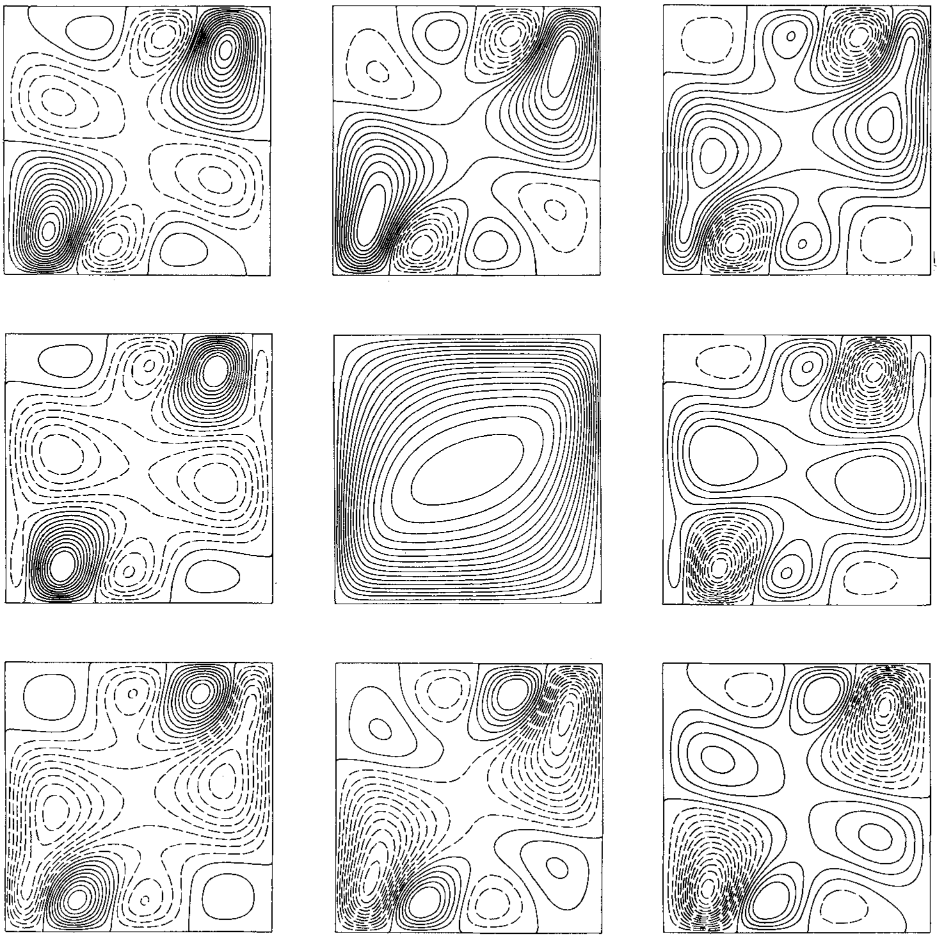

FIGURE 2(*a*). For caption see next page.

period. Surpluses of vorticity which correspond to clockwise rotation and surpluses in temperature are indicated with solid lines. A superposition of vorticity and temperature disturbance fields shows that upflow streamline disturbances generally coincide with surpluses in temperature disturbances and downflow disturbances with deficits in temperature, confirming the interpretation that these are small convection cells superimposed on the base flow. The disturbances strengthen while traversing the surfaces of heat transfer and weaken along the adiabatic surfaces.

At any instant, temperature and vorticity disturbances satisfy an antisymmetry and symmetry, respectively, through the centre of the box which is inherited from the base flow,

$$-\hat{\theta}(-x,\ -y) = -\hat{\theta}(x,\ y),$$

$$+\hat{\omega}(-x,\ -y) = +\hat{\omega}(x,\ y).$$

We need only refer to properties on half the box, the triangle formed by cutting the box along a diagonal, say. There are four vorticity disturbances identified by their centres and it takes four oscillation periods for one to travel completely around the box. On the other hand, there are five thermal disturbances and each one requires

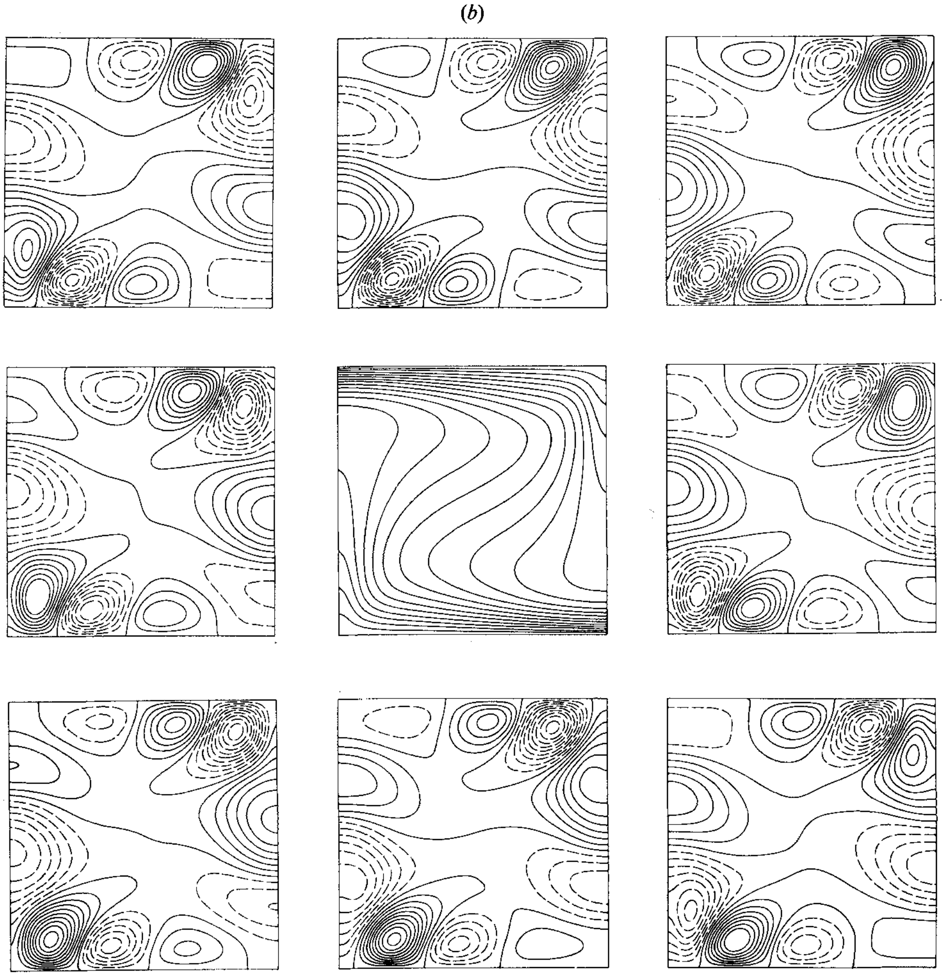

FIGURE 2. The disturbance streamlines (*a*) and isotherms (*b*) plotted at eight equal intervals of one oscillation period with time progressing in the clockwise sense. The base-state streamlines (*a*) and isotherms (*b*) are plotted at the centre; circulation of the streamlines is clockwise.

five periods to return to its original position. Thus, the average wave speed of the deviations in vorticity is $\frac{5}{4}$ that of thermal disturbances and in every cycle the thermals 'slip' relative to the vorticity deviations. This occurs along the adiabatic sidewall and can best be understood using the relationship between vorticity disturbance $\hat{\omega}$ and temperature disturbance $\hat{\theta}$,

$$\hat{\omega} = -R^{\frac{1}{2}}\frac{\partial \hat{\theta}}{\partial x}, \tag{11}$$

obtained by taking the curl of (10*b*). At the centre of a thermal disturbance,

$$\left(\frac{\partial \hat{\theta}}{\partial x}, \frac{\partial \hat{\theta}}{\partial y}\right) = (0, 0),$$

so that thermal centres necessarily lie along on a locus of points where the vorticity is zero. Since $\partial\hat{\theta}/\partial y \neq 0$ in general along the horizontal heat-transfer surfaces the

(a)

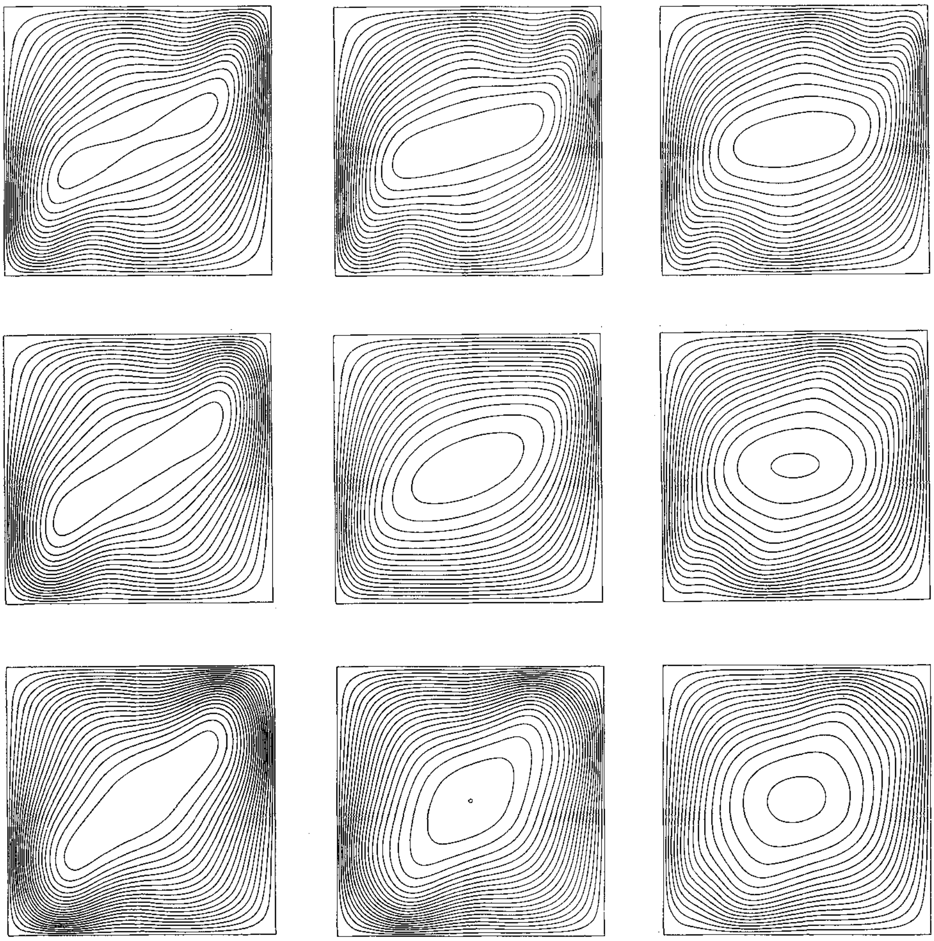

FIGURE 3(*a*). For caption see next page.

thermal centres are forced away from the wall to the internal boundaries between vorticity cells, whereas along the adiabatic surfaces these centres can also be at the wall. As evident from figure (2*b*) wall-bound disturbances do occur, and for these a vorticity disturbance can 'pass' the thermal disturbance.

The flow field and isotherms seen in experiment or via conventional numerical simulation for R above but close to oscillation onset are a superposition of the disturbances of figure 2 on the base states. This influence of the disturbances is shown in figure 3 for an arbitrarily chosen value of ϵ in (9), $\epsilon = 0.08$. A comparison with the flow fields reported by Caltagirone (1975), his figure 6, Frick & Muller (1983), their figure 2, and Kimura *et al.* (1986), their figure 3, for Rayleigh numbers significantly above R_{p} yields not only a quick qualitative identification of these instabilities but suggests that the linear superposition gives a good approximation for a wide range of $R > R_{\mathrm{p}}$.

The exact disturbance solution, figure 2, clearly shows the instability as one in which thermal 'blobs' or regions of excess temperature detach from the bottom surface, grow in size while diffusing in strength as they move vertically across the layer, reach the top surface and begin to strengthen and contract as they move

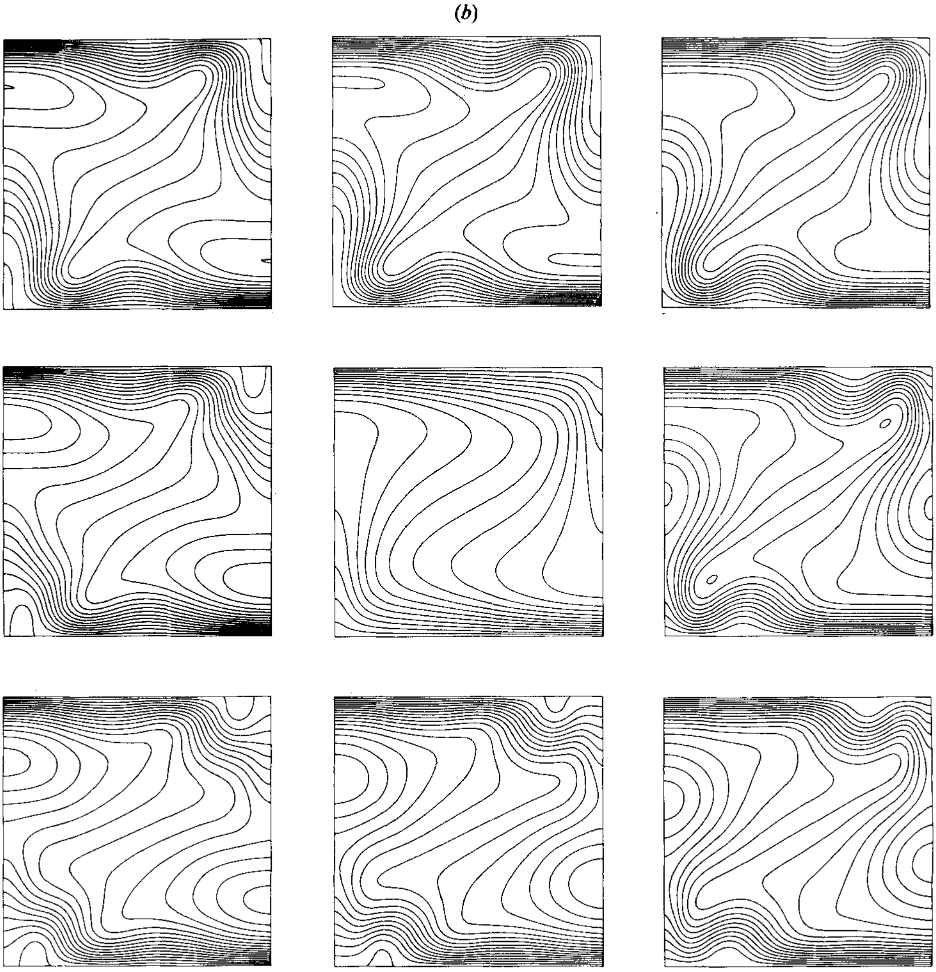

FIGURE 3. Streamlines (a) and isotherms (b) constructed by superposing the disturbance field with amplitude $\epsilon = 0.08$ on the base-state field (centre plot). The progression in time is clockwise shown at the same intervals as in figure 2.

horizontally. Both thermal-layer instability and cyclic triggering are part of the process; to this extent the conclusions of earlier studies are confirmed. On the other hand, the role of the base-state thermal boundary layer is still unclear. What determines the critical strength it must reach before a disturbance will persist and propagate? Note that detachement from the horizontal surface actually occurs at the wall where base-state gradients are the weakest suggesting that the 'triggering' mechanism due to the turning base flow (confinement by the wall) may be relatively more important. What determines the characteristic size (wavenumber) of the disturbance? Are the thermal disturbances, the vorticity disturbances, or neither convected with the base flow? These questions are answered by the more detailed analysis of the next sections in which a model of the disturbances as structures determined independently of their propagation is developed.

$\Omega_p t =$	0	$\frac{1}{4}\pi$	$\frac{1}{2}\pi$	$\frac{3}{4}\pi$
$\frac{1}{2}\mathrm{d}/\mathrm{d}t\langle\theta^2\rangle$	6.00	−9.16	−6.00	9.16
$-R^{\frac{1}{2}}\langle\theta \boldsymbol{v}\cdot\nabla\bar{\theta}\rangle$	50.29	45.90	44.40	48.70
$R^{\frac{1}{2}}\langle\theta \boldsymbol{v}\cdot\boldsymbol{k}\rangle$	95.90	86.25	82.78	92.40
$-\langle(\nabla\theta)^2\rangle$	−140.40	−141.50	−133.30	−132.20

TABLE 4. Contributions of the exact solution for the square box to the spatially averaged energy equation (13) at several instants during the oscillation period

5. Structure–propagation decomposition

The disturbance equation (10*c*) can be re-expressed as

$$\frac{\partial\theta}{\partial t}+R^{\frac{1}{2}}\bar{\boldsymbol{v}}\cdot\nabla\theta=\Phi, \tag{12a}$$

$$\nabla^2\theta-R^{\frac{1}{2}}\boldsymbol{v}\cdot(\nabla\bar{\theta}-\boldsymbol{k})=\Phi, \tag{12b}$$

where the hats on the disturbance quantities have been dropped, and where the function Φ represents the coupling between the 'propagation' equation (12*a*) and the 'structure' equation (12*b*). We outline the evidence from the exact solution that suggests that the coupling is relatively small. This evidence comes from several sources: a spatially averaged balance, a pointwise balance and a scaling balance which is implied by (12*a*), to be discussed at the end of this section.

The spatially averaged equations are obtained by multiplying (12*a*) and (12*b*) by θ, integrating over the box, denoted by $\langle\cdot\rangle$, and using the boundary conditions to obtain

$$\frac{1}{2}\frac{\mathrm{d}}{\mathrm{d}t}\langle\theta^2\rangle=\langle\theta\Phi\rangle, \tag{13a}$$

$$-\langle(\nabla\theta)^2\rangle-R^{\frac{1}{2}}\langle\theta\boldsymbol{v}\cdot\nabla\bar{\theta}\rangle+R^{\frac{1}{2}}\langle\theta\boldsymbol{v}\cdot\boldsymbol{k}\rangle=\langle\theta\Phi\rangle. \tag{13b}$$

Table 4 lists the magnitudes of the terms in (13) evaluated at the exact solution. The coupling term $\langle\theta\Phi\rangle$ always contributes less than 7 % of the largest term (the thermal dissipation $\langle(\nabla\theta)^2\rangle$).

At a fixed time, a pointwise evaluation of Φ shows that, except in the centre of thermal disturbances where $\nabla\theta$ is small, and in the stably stratified core region where $\bar{\boldsymbol{v}}$ is small, Φ is less than 10% of the largest contributing term in (12).

This empirical evidence leads us to neglect the coupling between the first-order wave equation (12*a*) and the elliptic equation (12*b*), consistent with the goal of a first approximation to the physics. With $\Phi=0$, (12*a*) can be rewritten in terms of the speed along a base-state streamline v' and the temperature variation along the streamline measured by the coordinate s,

$$\frac{\partial\theta}{\partial t}+R^{\frac{1}{2}}v'\frac{\partial\theta}{\partial s}=0. \tag{14}$$

Since, in general, v' is not constant along streamlines, this equation determines a distortion of disturbance θ; it does not involve propagation only. Furthermore, the evolution determined by (14) along various streamlines may not be compatible with (12*b*) with $\Phi=0$. Neglecting Φ makes the system overdetermined and no longer well posed.

h	α	$\Omega_{\mathrm{p}}\, h/R_{\mathrm{p}}^{\frac{1}{2}}\psi_{\max}\, \alpha$	R_{p}^{*}
0.50	5.0	9.16	330.3
0.67	5.0	7.96	353.1
0.75	5.0	7.90	364.4
1.00	5.0	7.88	390.7
1.50	5.0	7.72	428.5

TABLE 5. The scaling predicted by the propagation equation (15) evaluated using the exact solution is shown in column 3. Wavenumbers α are measured from the exact solutions. The critical Rayleigh number R_{p}^{*} defined to be the value R^{*} (equation (21*d*)) corresponding to $R = R_{\mathrm{p}}$ is listed in column 4.

On the other hand, there is only a difference of a factor of three between maximum and minimum speeds along the same streamline away from the walls suggesting that the influence of (14) on evolution (distortion) may be relatively small. In what follows we assume some typical streamline exists along which

$$\frac{\partial\theta}{\partial t}+R^{\frac{1}{2}}v^{*}\frac{\partial\theta}{\partial s}=0, \tag{15}$$

where v^{*} is the average velocity around the streamline (a constant), and along which a one-dimensional version of (12*b*) with $\Phi = 0$ applies. With these changes a well-posed system is recovered whereby the time-independent equation delivers the disturbance structure which can then be treated as an initial condition in the propagation equation (15).

As a check on the approximation of (15) we use the exact solution to scale the terms in (15) as they depend on aspect ratio h and examine the balance of these terms. We write estimates

$$\frac{\partial\theta}{\partial t}\sim\tilde{\theta}\Omega_{\mathrm{p}},\quad v^{*}\sim 2\psi_{\max}/h,\quad \frac{\partial\theta}{\partial s}\sim\tfrac{1}{2}\alpha\tilde{\theta}$$

where $\tilde{\theta}$ is a characteristic magnitude of the disturbance, Ω_{p} is the frequency of oscillation, $\psi_{\max}$ is the maximum value of the stream function, and α is the wavenumber of the disturbance along the characteristic streamline. The values Ω_{p} and $\psi_{\max}$ are known from the solution and α is the integer corresponding to the number of pairs of thermal cells as measured from figure 2(*b*) and analogous plots for the other aspect ratios. In column 3 of table 5, the ratio of the two terms in (15) are compared for various aspect ratios. Excluding the case $h = 0.5$, the ratios are within 4% of one another suggesting they are independent of h, as is necessary for (15) to be a reasonable approximation. Examination of the disturbance structure for $h = 0.5$ shows that, in contrast to other geometries considered, the sidewalls are so close that the ascending and descending vorticity disturbances are significantly distorted as they pass one another. We suspect that this interaction destroys the balance implied by (15).

In summary, we argue from the numerical solution that as a first approximation the propagation of the disturbance is independent of the balance determining the structure of the disturbance ($\Phi \equiv 0$ in equation (12)). The propagation can then be modelled as a one-dimensional wave equation with constant coefficients on some characteristic streamline loop. To close the model system a one-dimensional version of (12*b*) on the same domain is needed. The next two sections are devoted to the development of this approximation.

6. Model I

The decoupled structure equation ((12*b*) with $\Phi = 0$) with disturbance velocity eliminated through the momentum equation (10*b*) is written

$$\nabla^2\theta - R\theta(\nabla\bar{\theta}\cdot\boldsymbol{k} - 1) + R^{\frac{1}{2}}\nabla p\cdot(\nabla\bar{\theta} - \boldsymbol{k}) = 0. \tag{16}$$

To transform (16) from a two-dimensional rectangular domain to a one-dimensional loop domain in a rational way requires some averaging procedure which eliminates variations locally orthogonal to the loop coordinate. However, this may not be possible, at least in a uniform way, since, for example, conduction orthogonal to the streamline cannot be neglected at the centre of the thermal disturbance cells. This might require a transformation to an annulus or to a loop with 'thickness'. Various techniques are available for a rational reduction of dimension and transplantation of domain; these include the multiple-scales (spatial) and 'director' theory approach (e.g. Ericksen & Truesdell 1958) and either of these might be rigorously justified through a centre-manifold result for elliptic equations as has been successful for Saint-Venant problems (Mielke 1987). However, we already have an exact solution and since the aim of our model is to interpret that solution the *ad hoc* approach will suffice.

In this spirit we build a first model, Model I, by assuming that the contribution of the pressure gradient to the disturbance velocity is small relative to the contribution of the buoyancy term. Consequently, the third term in (16) is small relative to the second term and we shall neglect it for the time being. The derivative $\partial\bar{\theta}/\partial y$ is assumed given as a function of x and y and therefore can be evaluated on a loop domain; we are left with only the task of transforming the Laplacian term to the loop variable.

We first specialize the loop to a circle marked by the coordinates $0 \leqslant \zeta < 2\pi$ thereby neglecting the asymmetry about the box midline which the 'typical' streamline must possess (figure 2*a*, centre). A correspondence between the Laplacian and the second-order derivative $\mathrm{d}^2\theta/\mathrm{d}\zeta^2$ is assumed,

$$\nabla^2\theta = \beta^2\frac{\mathrm{d}^2\theta}{\mathrm{d}\zeta^2}, \tag{17a}$$

where the scaling factor β^2 varies with the aspect ratio and wavenumber. To determine the dependence of β^2 on h the single roll-cell disturbance on the rectangular domain and the disturbance on the circle with wavenumber unity are identified. The roll-cell (equation (5*i*), $i = [1, 1]$) solves the equation

$$\nabla^2\theta = -\pi^2\left(\frac{1}{h^2}+1\right)\theta, \tag{17b}$$

with the boundary conditions of the original system (1), and the corresponding disturbance on the circle solves

$$\frac{\mathrm{d}^2\theta}{\mathrm{d}\zeta^2} = -\theta, \tag{17c}$$

with periodic boundary conditions. Comparing (17*b*) and (17*c*) shows β^2 is proportional to $\pi^2(1/h^2+1)$. The constant of proportionality is unity for the single cell and decreases from unity as the wavenumber of θ increases; the dependence is weak. We evaluate it using the exact solution at $R_\mathrm{p} = 390$ and fix its value for the

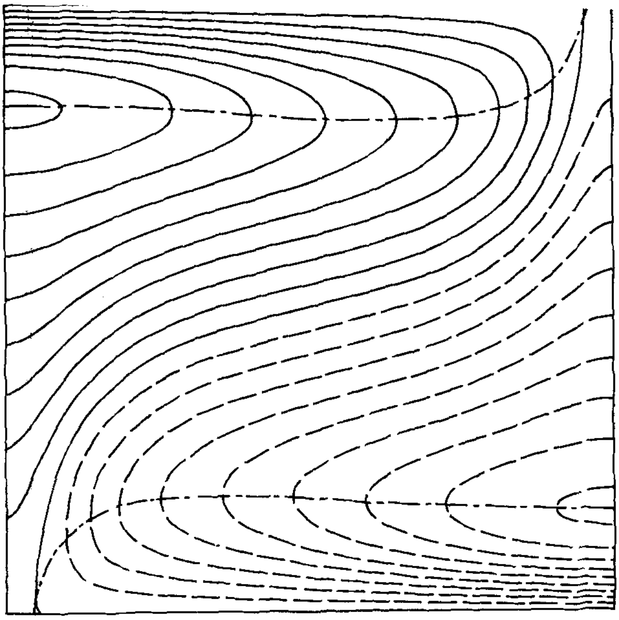

FIGURE 4. Isotherms of the steady-state temperature field relative to the linear conduction profile at the onset of the oscillatory instability. Solid lines represent surpluses and dashed lines deficits from the linear profile. Level curves are at intervals $\Delta\bar{\theta} = 0.06$ and $|\bar{\theta}|_{\max} = 0.56$. The dot-dashed lines are the locus of vanishing vertical temperature gradient ($\partial\bar{\theta}/\partial y = 0$).

rest of the analysis. An average of β^2, weighted by amplitude, for the ten largest contributions to the disturbance eigenvectors (table 2) leads to

$$\beta^2 \equiv 0.75\pi^2\left(\frac{1}{h^2}+1\right). \tag{18}$$

Model I can now be written

$$\beta^2\frac{\mathrm{d}^2\theta}{\mathrm{d}\zeta^2}+R\theta\left(1-\frac{\partial\bar{\theta}}{\partial y}(\zeta)\right)=0, \tag{19}$$

where periodicity of θ and $\mathrm{d}\theta/\mathrm{d}\zeta$ in ζ are the boundary conditions. Equation (19) is a Mathieu–Hill equation whose well-known properties include the existence of periodic solutions for discrete values of R only.

The remainder of this section is devoted to solving (19) for typical $\bar{\theta}$-fields. As noted in the discussion of the exact solution, both base-state temperature field and disturbances share an antisymmetry with respect to the centre of the box. We incorporate this symmetry in Model I restricting to $0 \leqslant \zeta < \pi$ with antisymmetric boundary conditions. The periodic function $\partial\bar{\theta}/\partial y(\zeta)$ can be deduced from the exact solution $\bar{\theta}(x, y)$ which is shown in figure 4 for $R_{\mathrm{p}} = 390.7$. Along a typical streamline (one that passes near the centres of the disturbance isotherms) $\partial\bar{\theta}/\partial y$ has two zeros for $0 \leqslant \zeta < \pi$ and a 'sawtooth' shape. We write this function as an amplitude A times the shape f,

$$\frac{\partial\bar{\theta}}{\partial y} = Af(\zeta), \tag{20a}$$

where

$$f(\zeta) \equiv \gamma^{-1}[\sin 2\zeta+\tfrac{1}{2}\sin 4\zeta+\tfrac{1}{3}\sin 6\zeta], \tag{20b}$$

$$\gamma \equiv \max_{\zeta}|\sin 2\zeta+\tfrac{1}{2}\sin 4\zeta+\tfrac{1}{3}\sin 6\zeta|, \tag{20c}$$

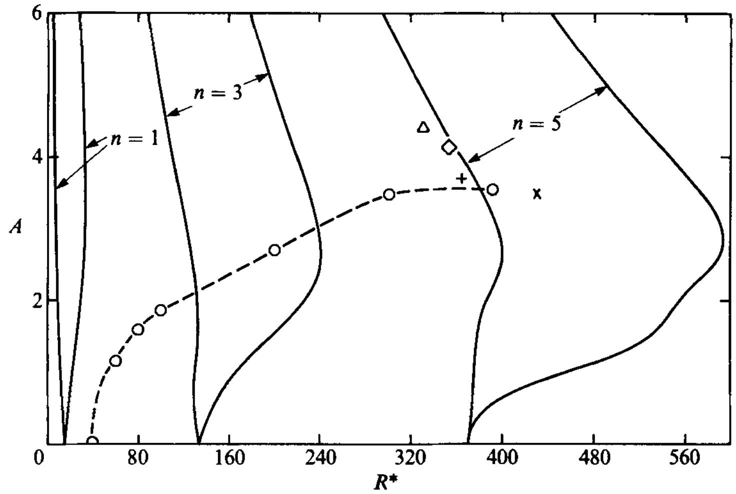

FIGURE 5. The locus of periodic solutions predicted by Model I (solid lines) with the results from the exact solution for various aspect ratios: △, $h = 0.5$; ◇, 0.67; +, 0.75; ○, 1.0; ×, 1.5. The dashed curve is the function $A(R^*)$ estimated from the isotherms of the exact solution (circles) for the square box.

and

$$A \equiv \max_{(x,y)} \left|\frac{\partial \bar{\theta}}{\partial y}\right|. \tag{20d}$$

The amplitude A is treated as a parameter; it must vary with aspect ratio as well as R. The angle ζ is measured clockwise from the diagonal which intersects the upper right corner of the square. A final change of independent variable, $\zeta \equiv \pi z$, brings (19) into the form

$$\frac{\mathrm{d}^2\theta}{\mathrm{d}z^2}+0.67R^*\theta(1-Af(\pi z)) = 0, \tag{21a}$$

$$\theta(0) = -\theta(1), \quad \frac{\mathrm{d}\theta}{\mathrm{d}z}(0) = -\frac{\mathrm{d}\theta}{\mathrm{d}z}(1), \tag{21b, c}$$

where

$$R^* \equiv \frac{2R}{1/h^2+1}. \tag{21d}$$

Equation (21) has periodic solutions with $n = 1$, 3 and 5 zeros for the parameter pairs (A, R^*) shown in figure 5. The 'tongues' which reach down to just touch the R^*-axis are typical of this well-known class of equations often studied in the context of parametrically excited oscillators. At $R^* = 390.7$ the only structures to fit on the full circle for small to moderate A have wavenumber $n = 5$ in correspondence with results for the square box. The scaled critical Rayleigh parameter R_p^* for the range of aspect ratios is listed in the last column in table 5. At each of the geometries, (21) by way of figure 5 predicts a structure with wavenumber $n = 5$ in agreement with the exact solutions. We note, however, that this scaling of the 'measured' R_p-values is not expected to bring them into coincidence. As suggested by (21) it includes the influence of h on thermal diffusion of disturbances but *not* on the critical strength of the base state $\bar{\theta}$. Only if the critical strength of the base-state thermal boundary layer were independent of h would the scaling (21d) be expected to map the R_p-values on to one another. As expected physically and as suggested by the 'measured' points on figure 5 the taller the box the greater the boundary-layer strength required for instability.

From figure 5, at $R^* = R^*_\mathrm{p}$ there are several values of A for which periodic solutions 'fit' on the circle. One of these values compares favourably in order of magnitude with the value of $|\partial\bar{\theta}/\partial y|_{\max}$ from the exact solution for $h = 1$. In the light of the approximations embodied in it, a prediction of the wavenumber is all that can be reasonably expected of the model. For example, we know that the thermal-disturbance structure evolves significantly throughout the cycle (figure 2) while the structure predicted by (21) propagates without distortion by the model; hence any similarity of structure predicted by (21) with that of the exact solution (at some particular instant) would be fortuitous. Therefore, we do not present the structures.

Although Model I suggests how the disturbance wavenumber can be accounted for if the critical value R_p is known, it leaves unanswered the more important question 'what determines R_p?'

7. Model II

The structure–propagation decomposition is evidently a consequence of the oscillatory instability; in other words, it is a condition necessary in order that the instability occur. This section tests the idea that the decoupling of structure and propagation may be the defining characteristic of the unstable disturbances (i.e. a sufficient condition). If so, it could be used to predict the destabilizing oscillations. In other words, suppose that a necessary and sufficient condition for the instability is that the structure equation (16) be satisfied. Then, given the function $\nabla\bar{\theta}$ as it changes with increasing R from convection onset, the value $R = R_\mathrm{p}$ would appear as the first value at which (16) could be satisfied; $R = R_\mathrm{p}$ would be the first eigenvalue of (16). In the context of Model I for fixed aspect ratio, the thermal-boundary-layer strength is known as a function of the Rayleigh number in the form $A(R^*)$. This function can be plotted on figure 5 and the first intersection with increasing R^* of this curve with a 'tongue' represents the point of instability. By this construction Model I predicts instability with wavenumber $n = 3$ and at a Rayleigh number R^* far below the observed value. However, Model I neglects the contribution of the pressure field to the disturbance velocity without justification. We now remedy this deficiency in order to make the model more predictive.

The pressure-field convection term of (16) can be split into two contributions,

$$R^{\frac{1}{2}}\frac{\partial p}{\partial y}\left(\frac{\partial\bar{\theta}}{\partial y}-1\right)+R^{\frac{1}{2}}\frac{\partial p}{\partial x}\frac{\partial\bar{\theta}}{\partial x}. \tag{22}$$

The second term is much smaller than the first for the range of R of interest since $\partial\bar{\theta}/\partial x \leqslant \partial\bar{\theta}/\partial y$ over most of the box (cf. figure 4), and where $\partial\bar{\theta}/\partial x$ is relatively large $\partial p/\partial x$ is small. Consequently, Model II neglects this contribution.

Properties of $\partial p/\partial y$ will be developed with the aim of transplanting that term to the circle domain. The idea to use the form of the Fourier series expression for $\partial p/\partial y$ as a function of the temperature disturbance θ to motivate the form for the transplanted functional in terms of the corresponding Fourier expansion on a circle domain. Recall that the pressure disturbance is a linear functional of the temperature disturbance and that the integral operator of (4) can be expressed explicitly in a Fourier expansion. Using this expansion the action of $\partial p/\partial y$ on a temperature disturbance θ, written in terms of the basis functions ($5i$),

$$\theta = \sum_{i=1}^{\infty} C_i \theta_i, \tag{23}$$

yields

$$F[\theta] \equiv R^{-\frac{1}{2}} \frac{\partial p}{\partial y} = \sum_{i=1}^{\infty} \left(\frac{\alpha_{yi}}{\alpha_i}\right)^2 C_i \theta_i, \tag{24}$$

where

$$\nabla^2 \theta_i = -\alpha_i^2 \theta_i \tag{25a}$$

and

$$\frac{\partial^2 \theta_i}{\partial y^2} = -\alpha_{yi}^2 \theta_i, \quad i = 1, 2, \ldots \tag{25b}$$

serve to define the wavenumbers α_i and α_{yi}. We note that the following two properties of F, which are readily apparent, hold for all θ satisfying the boundary conditions:

$$|F[\theta]| \leqslant |\theta| \quad \text{since} \quad |\alpha_{yi}| < |\alpha_i| \quad \text{for all } i, \tag{26a}$$

$$\langle \theta F[\theta] \rangle \geqslant 0. \tag{26b}$$

F can be re-expressed using the orthogonality of the basis functions ($5i$) which are elements of a Fourier series,

$$F[\theta] = \frac{4}{h} \sum_{i=1}^{\infty} \left(\frac{\left\langle \dfrac{\partial^2 \theta}{\partial y^2}, \theta_i \right\rangle}{\langle \nabla^2 \theta, \theta_i \rangle} \right) \langle \theta, \theta_i \rangle \, \theta_i. \tag{27}$$

The qualitative behaviour of the functional F is most apparent from the representation (24). Two influences can be distinguished. First, the rescaling of the components causes a phase shift. To see this consider $\theta = \theta_a + \theta_b$, where θ_a and θ_b are eigenfunctions from the set ($5i$) with wavenumbers $a = [2, 4]$ and $b = [4, 2]$, for example. Now,

$$5F[\theta_a + \theta_b] = 4\theta_a + \theta_b, \tag{28}$$

which gives a shift from a structure with equal parts θ_a and θ_b to one with parts in the ratio 4:1. A sketch of the corresponding roll-cell structures shows a phase shift of cells around the square; regions of upflow and downflow are interchanged. The second influence of F is the accentuation of the wavenumber in the vertical direction; the pressure gradient induced by the requirement of continuity significantly influences structures along the vertical walls, in contrast to the buoyancy force which dominates structures along the horizontal surfaces.

To transplant to the new domain representation (27) is most convenient. The functions θ_i ($5i$) transform to Fourier functions on the circle, $0 \leqslant \zeta \leqslant 2\pi$,

$$\theta_{sl} = \pi^{-\frac{1}{2}} \sin l\zeta, \tag{29a}$$

$$\theta_{cl} = \pi^{-\frac{1}{2}} \cos l\zeta, \quad l = 1, 2, 3, \ldots, \tag{29b}$$

where the constant θ_0 does not appear since its analogue in the square domain is prohibited by boundary conditions. Convolution functionals of θ are introduced:

$$\bar{\theta}_{sn} \equiv \pi^{-1} \int_0^{2\pi} \sin n(\zeta - t)\, \theta(t)\, \mathrm{d}t, \tag{30a}$$

$$\bar{\theta}_{cn} \equiv \pi^{-1} \int_0^{2\pi} \cos n(\zeta - t)\, \theta(t)\, \mathrm{d}t, \quad n = 1, \ldots, \infty. \tag{30b}$$

The sum of cosine transforms reproduces the Fourier expansion of θ,

$$\theta(\zeta) = \sum_{n=1}^{\infty} \bar{\theta}_{cn}(\zeta) = \sum_{n=1}^{\infty} (a_n \theta_{sn} + b_n \theta_{cn}), \tag{31a, b}$$

and the sine transform shifts the phase of each component of θ by $\frac{1}{2}\pi$,

$$\theta_{\frac{1}{2}\pi}(\zeta) \equiv \sum_{n=1}^{\infty} \bar{\theta}_{sn}(\zeta) = \sum_{n=1}^{\infty} (b_n \theta_{sn} - a_n \theta_{cn}), \tag{31c, d}$$

Only under special symmetries does the functional $\theta_{\frac{1}{2}\pi}(\zeta) = \theta(\zeta - \frac{1}{2}\pi)$; nevertheless, the action of $\theta_{\frac{1}{2}\pi}$ produces a phase distortion while preserving the norm. We exploit this phase action and introduce the approximation (consistent with (17*a*))

$$\frac{\partial^2 \theta}{\partial y^2} \sim \lambda \beta^2 \frac{\mathrm{d}^2 \theta_{\frac{1}{2}\pi}}{\mathrm{d}\zeta^2}, \tag{32}$$

in order to replace

$$\left\langle \frac{\partial^2 \theta}{\partial y^2} \theta_i \right\rangle, \quad i = 1, \ldots, \infty \tag{33}$$

with

$$\lambda \beta^2 \int_0^{2\pi} \left(\frac{\mathrm{d}^2}{\mathrm{d}\zeta^2} \theta_{\frac{1}{2}\pi} \right) \theta_{s,cl} \, \mathrm{d}t, \quad l = 1, \ldots, \infty. \tag{34}$$

The factor λ in (32) arises because $\partial^2\theta/\partial y^2$ is a fraction of $\nabla^2\theta$ which is known at convection onset ($\lambda = \frac{1}{2}$) and which can be estimated at oscillation onset from table 2 ($\lambda = 0.6$). However, we shall treat λ as a control parameter which measures the strength of the influence of $\partial p/\partial y$. Using (17*a*) again, (27) transplants to

$$F_{\frac{1}{2}\pi}[\theta] \equiv \lambda \sum_{s,c} \sum_{n=1}^{\infty} \left\{ \int_0^{2\pi} \left(\frac{\mathrm{d}^2}{\mathrm{d}\zeta^2} \theta_{\frac{1}{2}\pi} \right) \theta_{s,cn} \, \mathrm{d}t \Big/ \int_0^{2\pi} \frac{\mathrm{d}^2 \theta}{\mathrm{d}\zeta^2} \theta_{s,cn} \, \mathrm{d}t \right\} \left(\int_0^{2\pi} \theta \theta_{s,cn} \, \mathrm{d}t \right) \theta_{s,cn}(\zeta) \tag{35a}$$

$$= \lambda \theta_{\frac{1}{2}\pi}(\zeta). \tag{35b}$$

Equation (35*b*) follows from (35*a*) using the properties of Fourier expansion (31*b*, *d*). An arbitrary phase shift can be accommodated by generalizing (31),

$$\theta_{\delta n} \equiv \sin \delta \bar{\theta}_{sn} + \cos \delta \bar{\theta}_{cn}, \quad n = 1, \ldots, \infty, \tag{36a}$$

and

$$\theta_\delta(\zeta) \equiv \sum_{n=1}^{\infty} \theta_{\delta n} = \sin \delta \theta_{\frac{1}{2}\pi} + \cos \delta \theta. \tag{36b, c}$$

This leads to the generalization of F,

$$F_\delta[\theta] \equiv \lambda \theta_\delta, \tag{37}$$

motivated by calculations analogous to those that lead to (35*b*).

Straightforward estimates show that

$$|F_\delta[\theta]| \leqslant \lambda |\theta|, \tag{38a}$$

$$\int_0^{2\pi} \theta F_\delta[\theta] \, \mathrm{d}\zeta \geqslant 0, \tag{38b}$$

to be contrasted with properties (26) of F. In order to illustrate a further property of F_δ we obtain a preliminary version of Model II. Use $R^{\frac{1}{2}} F_\delta$ to represent $\partial p/\partial y$ in (22), neglect the $\partial p/\partial x$-term, and transplant the other terms in (16) following Model I to obtain,

$$\beta^2\frac{\mathrm{d}^2\theta}{\mathrm{d}\zeta^2}+R(\theta-F_\delta[\theta])\left(1-\frac{\partial\bar{\theta}}{\partial y}\right)=0. \tag{39}$$

The phase-shift contribution to F_δ eliminates periodic solutions to (39) when $\partial\bar{\theta}/\partial y=0$. To see this, multiply (39) (with $\partial\bar{\theta}/\partial y=0$) by $\mathrm{d}\theta/\mathrm{d}\zeta$ and rearrange to find

$$\tfrac{1}{2}\beta^2\frac{\mathrm{d}}{\mathrm{d}\zeta}\left[\left(\frac{\mathrm{d}\theta}{\mathrm{d}\zeta}\right)^2+R\theta^2\right]=R\frac{\mathrm{d}\theta}{\mathrm{d}\zeta}F_\delta[\theta]. \tag{40}$$

Integrate (40) from $\zeta=0$ to $\zeta=\tfrac{1}{2}\pi$,

$$\tfrac{1}{2}\beta^2\left[\left(\frac{\mathrm{d}\theta}{\mathrm{d}\zeta}\right)^2+R(1-\lambda\cos\delta)\,\theta^2\right]_0^{2\pi}=R\lambda\sin\delta\int_0^{2\pi}\frac{\mathrm{d}\theta}{\mathrm{d}\zeta}\theta_{\frac{1}{2}\pi}\,\mathrm{d}y \tag{41}$$

and note that through properties of $\theta_{\frac{1}{2}\pi}$, (31*c*),

$$\int_0^{2\pi}\frac{\mathrm{d}\theta}{\mathrm{d}\zeta}\theta_{\frac{1}{2}\pi}\,\mathrm{d}t\geqslant 0, \tag{42}$$

where equality holds if and only if $\theta=0$. Equation (41) and inequality (42) show that for $\delta\neq 0,\pi$ the only periodic solution is the trivial solution. This contrasts with the behaviour of Model I which possesses periodic solutions for $A=0$ (the 'tongues' of figure 5 touch the R^*-axis).

The development so far has accounted for the phase-shift action of F through approximation (32) but has not included the accentuation of y-wavenumbers. To do so, parts of the circle must correspond to the vertical sides of the box. Since the reference $\zeta=0$ is the upper right diagonal, we take the intervals $0\leqslant\zeta\leqslant\tfrac{1}{2}\pi$ and $\pi\leqslant\zeta\leqslant\tfrac{3}{2}\pi$ to represent the vertical sidewalls. New convolution functionals of θ are introduced,

$$\tilde{\theta}_{sn}\equiv\pi^{-1}\int_0^{2\pi}k(t)\sin n(\zeta-t)\,\theta(t)\,\mathrm{d}t, \tag{43a}$$

$$\tilde{\theta}_{cn}\equiv\pi^{-1}\int_0^{2\pi}k(t)\cos n(\zeta-t)\,\theta(t)\,\mathrm{d}t, \tag{43b}$$

$$n=1,\,2,\,\ldots,\,\infty,$$

where $0\leqslant k(\zeta)\leqslant 1$ filters out wavenumber contributions from 'non-vertical' intervals of the box; it acts as a characteristic function of the intervals $0\leqslant\zeta\leqslant\tfrac{1}{2}\pi$ and $\pi\leqslant\zeta\leqslant\tfrac{3}{2}\pi$. The corresponding series are defined as

$$\tilde{\theta}(\zeta)\equiv\sum_{n=1}^{\infty}\tilde{\theta}_{cn}, \tag{44a}$$

and

$$\tilde{\theta}_{\frac{1}{2}\pi}(\zeta)\equiv\sum_{n=1}^{\infty}\tilde{\theta}_{sn}, \tag{44b}$$

The approximation for the quantity (33) may now be revised. The functional $\theta_{\frac{1}{2}\pi}$ in expression (34) is replaced by $\tilde{\theta}_{\frac{1}{2}\pi}$; this leads to a new transplantation of F,

$$\tilde{F}_{\frac{1}{2}\pi}[\theta]=\lambda\sum_{s,c}\sum_{n=1}^{\infty}\left\{\int_0^{2\pi}\left(\frac{\mathrm{d}^2}{\mathrm{d}\zeta^2}\tilde{\theta}_{\frac{1}{2}\pi}\right)\theta_{s,cn}\,\mathrm{d}t\Big/\int_0^{2\pi}\frac{\mathrm{d}^2\theta}{\mathrm{d}\zeta^2}\theta_{s,cn}\,\mathrm{d}t\right\}\left(\int_0^{2\pi}\theta\theta_{s,cn}\,\mathrm{d}t\right)\theta_{s,cn}(\zeta) \tag{45a}$$

$$=\lambda\tilde{\theta}_{\frac{1}{2}\pi}(\zeta). \tag{45b}$$

Equation (45*b*) follows from (45*a*) by Fourier expansion of θ in θ_{sl}, θ_{cl}, (29), definitions (43*a*), along with straightforward trigonometric manipulation. In a way analogous to the derivation of (37), $\tilde{F}$ is generalized to an arbitrary phase shift δ,

$$\lambda^{-1}\tilde{F}_{\delta}[\theta] = \tilde{\theta}_{\delta} \equiv \sin\delta\tilde{\theta}_{\frac{1}{2}\pi} + \cos\delta\tilde{\theta}. \tag{46a, b}$$

The following property of $\tilde{F}_{\delta}$, analogous to that of F, can be verified easily:

$$|\tilde{F}_{\delta}[\theta]| \leqslant \lambda|\theta|. \tag{47}$$

However, further properties of $\tilde{F}_{\delta}$ analogous to inequality (38*b*) or to inequality (42) are not direct. On the other hand, the behaviour of $\tilde{F}_{\delta}$ as reflected by the behaviour of Model II, obtained numerically and discussed below, shows that $\tilde{F}_{\delta}$ prohibits periodic solutions for $\partial\bar{\theta}/\partial y = 0$.

The final version of Model II uses $R^{\frac{1}{2}}\tilde{F}_{\delta}$ to represent $\partial p/\partial y$ in (22), and otherwise follows the development of the preliminary version, (37), to obtain

$$\beta^{2}\frac{\mathrm{d}^{2}\theta}{\mathrm{d}\zeta^{2}} + R(\theta - \tilde{F}_{\delta}[\theta])\left(1 - \frac{\partial\bar{\theta}}{\partial y}\right) = 0, \tag{48a}$$

$$\theta(0) = \theta(2\pi), \quad \frac{\mathrm{d}\theta}{\mathrm{d}\zeta}(0) = \frac{\mathrm{d}\theta}{\mathrm{d}\zeta}(2\pi). \tag{48b, c}$$

This linear integro–differential equation is the Mathieu–Hill equation (19) modified by the functional $\tilde{F}_{\delta}$. We expect its solutions to be somewhat perturbed from those of the Mathieu–Hill equation.

We examine a particular realization of Model II in order to illustrate the nature of the modifications that $\tilde{F}_{\delta}$ induces. As in the realization of Model I, the antisymmetry about the centre of the box is incorporated in the solution of the half-circle and reflected to the other half. We again choose $\partial\bar{\theta}/\partial y$ given by (20) and change variables, $\zeta = \pi z$, to obtain

$$\frac{\mathrm{d}^{2}\theta}{\mathrm{d}z^{2}} + 0.67R^{*}(\theta - \lambda[\cos\delta\tilde{\theta} + \sin\delta\tilde{\theta}_{\frac{1}{2}\pi}])\,(1 - Af(\pi z)) = 0, \tag{49a}$$

$$\theta(0) = -\theta(1), \quad \frac{\mathrm{d}\theta}{\mathrm{d}z}(0) = -\frac{\mathrm{d}\theta}{\mathrm{d}z}(1). \tag{49b, c}$$

In the realization of $\tilde{\theta}$, through definitions (43), we choose $k(z) = \sin^{2}(z + \frac{1}{4})$ which has the property $\frac{1}{2} \leqslant k(z)$ for $0 \leqslant z \leqslant \frac{1}{2}$ thereby emphasizing wavenumbers on the 'vertical' portions of the circle. The symmetry of k is consistent with boundary conditions (49*b, c*) provided the wavenumbers in the series, (44), are odd. In order to compute the characteristics of (49) the series (44)is truncated to terms with $n = 1, 3, 5, 7$.

The modified characteristics are plotted for $\delta = \frac{1}{2}\pi$ and $\lambda = 0.35$ in figure 6. Only the relevant tongues $n = 3$ and $n = 5$ are shown. The value of δ is chosen to illustrate the strongest influence of phase shift. The value of λ is the smallest value for which the tongues lift far enough off the axis so that no solutions (for $h = 1$) fit on the loop until the $A(R^{*})$-curve intersects the $n = 5$ tongue. As λ is further increased toward values comparable with estimates of λ from the exact solution ($0.5 \leqslant \lambda \leqslant 0.6$) the tongues lift further from the axis and the number of zeros of solutions on parts of the tongue boundaries are modified. What began as the $n = 3$ tongue develops pieces with five zeros and what was the $n = 5$ tongue has portions where there are seven

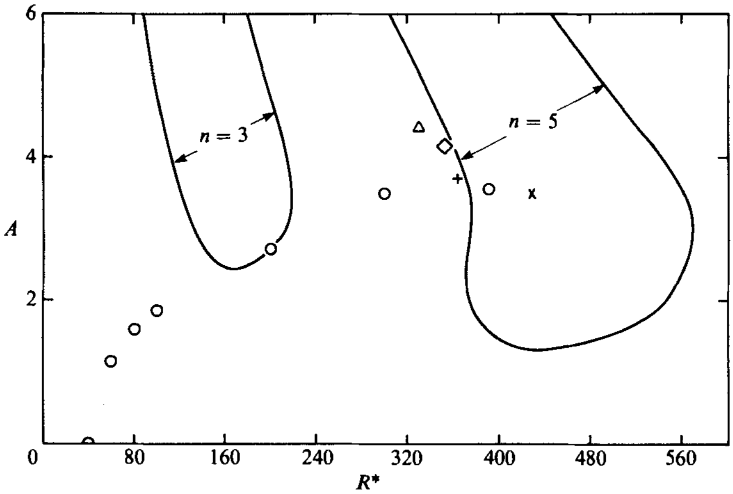

FIGURE 6. The locus of periodic solutions with $n = 3$ and $n = 5$ zeros predicted by Model II (solid lines) with parameter values $\lambda = 0.35$ and $\delta = \frac{1}{2}\pi$. Other symbols are as in figure 5.

zeros. Nevertheless, the $A(R^*)$-curve first crosses a tongue at an $n = 5$ solution and the qualitative result of figure 6 persists. As δ varies from $\frac{1}{2}\pi$ the tongues shift lower and slightly to the right or left. For $\delta = 0$ and $\delta = \pi$ the structure of figure 5 is recovered with a shift of the R^*-axis and a slight distortion due to $k(z)$.

The shape of the function $k(z)$ only weakly influences the pictures although the emphasis of the y-wavenumbers seems to accentuate the lifting action of the phase shift. The truncation of the convolution integrals (44) at term $n = 7$ has little effect on figure 6 as verified by lowering the truncation order to $n = 5$. The curves in figure 5 and 6 were calculated using the branch-tracing capability provided by the AUTO software.

8. Discussion and conclusions

The exact solution shows that five thermal disturbance cells circulate outside the nearly motionless core of the steady base flow which they destabilize. The correlation between base-state velocity, the wavelength of the thermal disturbance, and the oscillation frequency, presented in table 5, suggests that the thermal disturbances travel on average with the base flow. On the other hand, the four vorticity disturbances complete a cycle in the same time as the thermals and therefore travel with greater wave speed. Vorticity disturbances can pass the thermal disturbances along the adiabatic sidewalls whenever the centres of the thermals are located along the wall.

Evidence suggests that the travelling-wave instability is characterized by a nearly time-independent norm of its 'energy', an observation which may be useful in distinguishing the various oscillatory instabilities both calculated (Frick & Muller 1983) and recorded in experiment (Koster & Muller 1984). This weak coupling between the propagation of the disturbance and its structure suggests a mechanism in which the structure is determined independently, an idea developed through the framework of Models I and II.

Model I correlates thermal-disturbance size (wavenumber) with strength of the base-state thermal layer for various aspect ratios assuming a balance between dissipation of the cell by thermal diffusion and concentration of heat by convection due to disturbance velocity or, more precisely, that part of the disturbance velocity generated by the buoyancy force. The structure of Model I indicates that only certain Rayleigh numbers allow a balance between conduction and convection with a resulting cell size that will fit in the box. At these special Rayleigh numbers wavetrains on the circle with wavenumbers $n = 3, 5$, and so on can occur. According to the model they exist no matter what the strength of the base-state thermal layer A. Furthermore, even for a fixed strength A the size is not uniquely determined. However, by fixing the Rayleigh number at the values of R_{p} known from the exact solutions, the model gives thermal-layer strengths in good agreement with the exact values. This success of Model I suggest that it captures the dominant balance governing disturbance structure. This balance distinguishes the influence of the linear conduction profile, whose strength is proportional to Rayleigh number, and the steady-state boundary layer whose strength is measured by A. It shows that the Rayleigh number is of primary importance in generating buoyancy forces sufficient for convection velocities that can balance conduction. The strength A is a secondary influence. Nevertheless, Model I does not provide a complete explanation of wavenumber selection; it cannot explain, for example, why wavenumber $\alpha = 5$ rather than $\alpha = 3$ is realized physically.

In the case of the pure fluid layer infinite in horizontal extent with no-slip boundaries at top and bottom Bolton, Busse & Clever (1986) have calculated 'oscillatory blob' instabilities which, although strictly three-dimensional, have disturbance structures with a striking resemblance to those of figure 2. These blobs have wavenumbers which vary from 1 to 4 and for certain ranges of Prandtl number can be the most dangerous disturbances. These authors show plots of the structures for several wavenumbers but do not discuss the mechanism of wavenumber selection for this class of disturbances. Indeed, we do not know of any previous work in the context of the Rayleigh–Bénard, Hele-Shaw, or the porous-media problem that addresses the detailed physics of wavenumber selection.

Model II attempts to remedy deficiencies of Model I by accounting for the vertical pressure gradient. The gradient is a functional of the thermal disturbance field and has a concise expression in terms of its Fourier expansion. This exact representation shows that the pressure gradient shifts the phase of the disturbance cells with an amplitude dependent on the fraction of vertical to horizontal structure in the thermal field. Model II uses an approximation to the exact functional that preserves some average properties but that is neither a systematic nor a rational one. Nevertheless, it demonstrates how the pressure term might suppress the formation of disturbance cells for weak base-state thermal layers. In particular, if the thermal layer is not sufficiently strong the pressure field will disperse the cells along the vertical boundaries, weakening them to the extent that they cannot be sustained by the disturbance velocity. As the thermal-layer strength increases with Rayleigh number, the cells first fit on the circle with wavenumber $\alpha = 5$. Here, wavenumber selection depends directly on Rayleigh number through the conduction profile (owing to the constraint of the circular domain) and indirectly through the thermal-layer strength. The data from the exact solutions are not in disagreement with this picture. Yet the loose connection between model and the governing equations makes stronger statements inappropriate; we present this picture as a hypothesis.

The one-dimensional model, based on the exact integro-differential equation governing thermal disturbances, has several noteworthy features. Since the velocity field has been eliminated from the exact equation, transplantation of a vector field from the rectangle to the circle is circumvented. As a result, the coupling between momentum and energy is preserved in the simplicity of the one-dimensional model; we need not be concerned that the velocity induced by the one-dimensional temperature solution does not satisfy continuity on the one-dimensional domain. Other features of the model which distinguish it from conventional convection-loop models are the influence that the adiabatic sidewalls and the pressure field have on the dynamics as well as the dominant role of conduction in the direction of the loop coordinate.

In summary, we present evidence for a rather simple picture of instability and wavenumber selection. The decay of hot spots is balanced by self-induced buoyancy-driven convection to produce a cell size that will fit on a loop for certain Rayleigh numbers. The influence of the pressure gradient on the cells along the vertical sidewalls effectively enhances the diffusion and thereby stabilizes the flow to low-wavenumber disturbances when thermal-boundary-layer strengths are moderate.

The significance of these results may be viewed from several perspectives. It may be argued that the particular mechanism we outline is of limited relevance to higher instabilities in other flows because of rather special features of the porous-media problem (two-dimensional, Darcy's law, slippery walls, etc.). On the other hand, it is one of a few hydrodynamic contexts (problems) in which a detailed understanding of the interaction between non-trivial spatial structures and unsteady temporal behaviour has been developed and, moreover, the quadratic nonlinearity responsible for this interaction is in some sense a prototype nonlinearity for the class of hydrodynamic problems where convective nonlinearities dominate (including the convection of momentum). On the level of methodology, the branch-tracing approach (continuation) is flexible and can be generalized to capture higher-order transitions provided the dynamics of the bifurcating solution has a known mathematical structure (e.g. certain types of break-up of a torus and most transitions to chaos cannot be handled yet). Finally, on yet another level, our analysis might serve as an example in which a disciplined analytic modelling based on a numerical solution leads to a simplified physical picture; even reliable numberical solutions may be of little use on their own without 'post-modelling'.

We thank the reviewers for comments contributing to the quality of the paper and we thank Mike Graham for his help with the computations. This work was substantially supported by the National Science Foundation through grant MEA 84-11756 and was partly supported by the US Army Research Office through the Mathematical Sciences Institute of Cornell University. Numerical simulations reported here were performed at the Cornell National Supercomputer Facility, Center for Theory and Simulation in Science and Engineering, which is funded, in part, by the National Science Foundation, New York State, and the IBM Corporation.

REFERENCES

AIDUN, C. K. & STEEN, P. H. 1986 *AIAA/ASME 4th Joint Thermophysics and Heat Trans. Conf., AIAA paper* 86-1264.

AIDUN, C. K. & STEEN, P. H. 1987 *J. Thermophys.* **1**, 268.

BECK, J. L. 1972 *Phys. Fluids* **15** 1377.

BOLTON, E. W., BUSSE, F. H. & CLEVER, R. M. 1986 *J. Fluid Mech.* **164**, 469.

CALTAGIRONE, J.-P. 1974 *C. R. Acad. Sci. Paris* **278**, 259.

CALTAGIRONE, J.-P. 1975 *J. Fluid Mech.* **72**, 269.

Caltagirone, J.-P., Cloupeau, M. & Combarnous, M. 1971 *C. R. Acad. Sci. Paris* **273**, 833.

Combarnous, M. & LeFur, B. 1969 *C. R. Acad. Sci. Paris* **269**, 1009.

Doedel, E. J. 1980 AUTO: A Program for the Automatic Bifurcation Analysis of Autonomous Systems. In *Proc. 10th Manitoba Conf. on Numerical Math. and Comp.*, p. 265.

Eriksen, J. L. & Truesdell, C. 1958 *Arch. Rat. Mech. Anal.* **1**, 295.

Frick, H. & Clever, R. M. 1982 *J. Fluid Mech.* **114**, 467.

Frick, H. & Muller, U. 1983 *J. Fluid Mech.* **126**, 521.

Hartline, B. K. & Lister, C. R. B. 1977 *J. Fluid Mech.* **79**, 379.

Horne, R. N. & Caltagirone, J.-P. 1980 *J. Fluid Mech.* **100**, 385.

Horne, R. N. & O'Sullivan, M. J. 1974 *J. Fluid Mech.* **66**, 339.

Horne, R. N. & O'Sullivan, M. J. 1978 *Phys. Fluids* **21**, 1260.

Keller, H. B. 1977 Numerical Solution of Bifurcation and Nonlinear Eigenvalue Problems. In *Applications of Bifurcation Theory* (ed. P. H. Rabinowitz), p. 359. Academic.

Kimura, S., Schubert, G. & Straus, J. M. 1986 *J. Fluid Mech.* **166**, 305.

Kimura, S., Schubert, G. & Straus, J. M. 1987 *Trans. ASME J. Heat Transfer* **109**, 350.

Koster, J. N. & Muller, U. 1980 In *Natural Convection in Enclosures*, ASME HTD, vol. 8, p. 27.

Koster, J. N. & Muller, U. 1981 *Phys. Rev. Lett.* **47**, 1599.

Koster, J. N. & Muller, U. 1982 *J. Fluid Mech.* **125**, 429.

Koster, J. N. & Muller, U. 1984 *J. Fluid Mech.* **139**, 363.

Kvernvold, O. 1979 *Intl. J. Heat Mass Transfer* **22**, 395.

Lapwood, E. R. 1948 *Proc. Camb. Phil. Soc.* **44**, 508.

Mielke, A. 1987 *Mathematical Sciences Institute, Cornell University, Rep.* 87-25.

Rosenblat, S. 1979 *Stud. Appl. Maths* **60**, 241.

Schubert, G. & Straus, J. M. 1982 *J. Fluid Mech.* **121**, 301.

Steen, P. H. 1986 *Phys. Fluids* **29**, 925.